Robust Gust Load Alleviation at Different Flight Points and Mass configurations

Hugo Fournier, Paolo Massioni, Minh Tu Pham, Laurent Bako, Robin Vernay, Michele Colombo

Robust Gust Load Alleviation at Different Flight Points and Mass configurations

Hugo Fournier *
Airbus Operations SAS, 31060 Toulouse, France and INSA Lyon, F-69100 Villeurbanne, France

Paolo Massioni† and Minh Tu Pham‡
Univ Lyon, INSA Lyon, Université Claude Bernard Lyon 1, CNRS, Ampère, UMR5005, 69621 Villeurbanne, France

Laurent Bako §
Univ Lyon, Ecole Centrale de Lyon, CNRS, Ampère, UMR5005, 69130 Ecully, France

Robin Vernay ¶ and Michele Colombo ‖
Airbus Operations SAS, 31060 Toulouse, France

This work studies the gust load alleviation of a flexible aircraft equipped with a lidar sensor that measures the wind velocity ahead of the aircraft. The focus is put on the aeroelastic dynamics uncertainties due to the evolution of the velocity and the altitude during a flight, and to the variations of the aircraft mass configuration. A robust control approach is adopted in order to minimize the aircraft loads due to the wind in presence of such uncertainties with low-order controllers that satisfy the constraints imposed by the system's limitations and the implementability considerations. This is achieved through structured mixed H_2/H_∞ synthesis with multiple models. The load alleviation capability of controllers of various orders, using a variable number of control surfaces, is assessed through the computation of the maximum loads obtained in various conditions of velocity, altitude and mass configurations.

I. Introduction

The design of an aircraft is a multi-disciplinary process aiming at reducing the required fuel consumption for a given payload and range. It can be improved in different ways, by improving the engines efficiency or reducing the mass of the aeroplane whilst maintaining its overall capabilities. Using new lighter materials, but also in a less straightforward way reducing the maximum loads the aircraft has to withstand are the means to reduce the mass. For example, the wing spar is a heavy element, designed to withstand the maximum bending moment and shear force that will be created during the aircraft life cycle. One of the load sizing cases for the wing is the strong turbulence or gust.

*(Corresponding author) PhD Candidate, Flight Physics Department, Loads and Aeroelasticity Engineering, hugo.h.fournier@airbus.com
†Associate Professor
‡Associate Professor
§Associate Professor
¶Research and Development Engineer, Flight Physics Department, Loads and Aeroelasticity
‖Research and Development Engineer, Flight Physics Department, Loads and Aeroelasticity

With an adequate control law that uses the elevators, ailerons, and possibly new control surfaces [1], this load level can be strongly reduced, leading to significant mass savings and so to an overall performance improvement.

Several control strategies have been employed in the past for the design of such Gust Load Alleviation (GLA) control laws, starting with feedback control [2–5], based on the aircraft measured output, typically the pitch rate, yaw rate and vertical load factor obtained from gyroscopes and accelerometers. In order to improve the GLA performance, an additional feedforward controller that directly uses the measurement of the wind perturbation can be used in addition to feedback control [6–8] or used alone [9–11].

Developments of airborne lidar sensors in the last decades [12, 13] create new opportunities in Gust Load Alleviation by providing a measurement of the wind perturbation in phase advance. While simple controller structures are commonly used for feedback control, finding a controller structure that takes the wind predictions as input is not straightforward. Model Predictive Control (MPC) methods that perform an online optimization can be used, they have been applied to gust load alleviation [14, 15] and maneuver load alleviation [16, 17]. More complex strategies based on wavelet decomposition of the lidar signal have been used in order to map the signal onto the different actuators depending on the frequency and the amplitude of the gust [18, 19]. The H_∞ and μ syntheses [20–22] provide a frame compatible with lidar measurements, in which one can perform a multi-objective optimization while ensuring closed-loop stability and compliance with robustness constraints and system's limitations. Already used for robust GLA with classical sensors [23–25] and for active flutter suppression of flexible aircraft [26, 27], the application of H_∞ to lidar-based GLA has been proposed in [28] and [29].

Techniques such as MPC, dynamical inversion or Linear Quadratic Gaussian (LQG) control strongly depend on the model knowledge, and in case the aeroelastic system does not behave as the model used for design, the GLA performance can be decreased and instabilities can arise. In addition to modeling errors and over-simplifying hypotheses, important variations in the aircraft dynamics occur during a flight or between two flights, and can cause the true system to differ from the model used during the design phase. This particularity is due to the important variations of the aircraft's mass configuration depending on the fuel tanks filling and on the payload, and to the variations of the flight characteristics such as the velocity and altitude, that affect the aerodynamics and the atmosphere environment. While some parameters causing these variations are known, it is difficult to precisely model their effect on the various aeroelastic modes that compose the system. The main approach to deal with this important issue in GLA is to define adaptive control laws, generally relying on finite-impulse response controllers [9–11, 30–32], that can adapt in real-time to the current system thanks to the sensors' measurements. This technique is promising but requires an on-line optimization process that can be computationally intensive and does not lead to strong guarantees of stability and performance.

This work investigates the design of control laws that are easy to implement on today's on-board computers and that provide strong guarantees about the stability and the load alleviation performance, relying on the robust H_2/H_∞ framework [33]. It follows the work of [29] that assessed the robustness and performance of unstructured and structured

controllers that can reduce multiple loads in the aircraft due to the wind, using a lidar. It brings the following novelties that have not been exposed before:

- The design of a single robust controller able to reduce the maximum loads at different flight points and with different mass configurations.
- The actuators configuration is studied with an aircraft model that includes a high number of ailerons, covering the wing's trailing edge. It allows to study the influence of the ailerons size on the ability to reduce several loads simultaneously.

Section II presents the models of the aircraft aeroelastic dynamics and of the wind perturbation, with focus on the dependence on the flight parameters, whose ranges are clearly defined by a simplified flight domain, and on the mass configuration of the aircraft. Section III presents the H_2/H_∞ strategy used for designing a robust low-order controller able to reduce the loads on different aircraft models. Finally section IV shows times simulations of such controllers, and the loads envelopes obtained from multiple models are calculated with various ailerons configurations.

II. Model Description and objectives

A. Aeroelastic Model

The wind can create dynamical loads on an aircraft that add to the statical loads mainly due to the lift and drag of the wing. The effect of wind onto the whole structure can only be captured by modeling the interactions between the unsteady aerodynamics and the structural dynamics of the aircraft. In this work, a Finite Element Model (FEM) model is used to model the aircraft structure. It is coupled with an unsteady linear aerodynamic model obtained by Doublet Lattice Method (DLM). The two models are implemented on Nastran [34], which performs a reduction of the full model, initially expressed in geometrical coordinates with a high number of degrees of freedom, into a smaller model expressed in the so-called modal-coordinates. 80 structural modes are included in addition to the 6 flight dynamics modes corresponding to the rigid-body degrees of freedom, leading to the following aeroelastic equations

$$\left[\boldsymbol{M_{hh}}\, s^2 + \boldsymbol{B_{hh}}\, s + \boldsymbol{K_{hh}}\right] \boldsymbol{h} = \bar{q} \left[\boldsymbol{Q_{hh}}(M,k)\boldsymbol{h} + \boldsymbol{Q_{vh}}(M,k)\frac{\boldsymbol{v}}{V}\right] \tag{1}$$

where $\boldsymbol{h}$ are the generalized modal coordinates, including the flight dynamics and elastic degrees of freedom and the control surface deflection angles $\boldsymbol{u}$, $s = j\omega$, $\bar{q} = \frac{1}{2}\rho V^2$ is the dynamic pressure with ρ the air density and V the true airspeed (TAS), $M = V/a$ is the Mach number with a the local speed of sound, $\boldsymbol{M_{hh}}$ is the modal mass matrix, $\boldsymbol{B_{hh}}$ is the modal damping matrix, $\boldsymbol{K_{hh}}$ the modal stiffness matrix, $\boldsymbol{Q_{hh}}$ and $\boldsymbol{Q_{vh}}$ are the modal and turbulent forces, $\boldsymbol{v}$ is the wind velocity. The computation of the aerodynamic forces is performed at different Mach numbers M and reduced frequencies $k = \frac{\omega b}{V}$ with b the reference semi-chord and ω the angular frequency. The outputs of interest $\boldsymbol{y}$ are obtained

Aircraft property	Value
Wing span	70 m
Wing aspect ratio	13
Mean aerodynamic chord	7 m
Mass (min)	130.000 kg
Mass (max)	250.000 kg

Table 1 Properties of the XRF1-HAR aircraft

directly from the modal displacements by:

$$\boldsymbol{y} = \boldsymbol{H_y}(s)\boldsymbol{h} \tag{2}$$

where $\boldsymbol{H_y}(s)$ is a known transfer function matrix. The output variable $\boldsymbol{y}$ contains the loads and the sensors measurements:

$$\boldsymbol{y} = \begin{Bmatrix} \boldsymbol{y_{loads}} \\ \\ \boldsymbol{y_{sens}} \end{Bmatrix} \tag{3}$$

The computations are performed with the XRF1-HAR (High Aspect Ratio) model developed by Airbus for research purposes. Some of its characteristics are shown in Table 1.

It is worth emphasizing the dependence of the aeroelastic model upon the flight point parameters and the mass configuration. By assuming that the air density and the speed of sound are entirely determined by the altitude, like in the U.S. Standard Atmosphere model [35], then the Mach number, TAS, altitude and dynamic pressure are entirely determined by fixing only two of them. In this work, the Mach number and TAS are free parameters, that entirely determine the flight point. Furthermore, the structural matrices $\boldsymbol{M_{hh}}$, $\boldsymbol{B_{hh}}$ and $\boldsymbol{K_{hh}}$ are computed for a given configuration of the aircraft, that depends on the quantity of fuel in the tanks and on the aircraft payload. It can be seen in Table 1 that the maximum possible weight of the aircraft is almost twice that of the empty configuration, where no fuel and no payload are present. The whole structural dynamics of the aircraft is affected by the mass configuration, and for certification purposes, several configurations corresponding to different fuel tank filling and payload cases should be considered. In this work, sixteen different mass configurations are chosen.

Eqs (1) and (2) do not directly lead to a linear system, because of the nonlinear dependence of the generalized forces $\boldsymbol{Q_{hh}}$ and $\boldsymbol{Q_{vh}}$ on the angular frequency ω through the reduced frequency k. In order to obtain a linear state-space model with $[\boldsymbol{v}/V; \boldsymbol{u}]$ as input and $\boldsymbol{y}$ as output, a procedure similar to that of [29] is used: first equations (1) and (2) are evaluated at different frequencies to obtain frequency response data of the desired transfer function, then a MIMO system identification is performed based on the Loewner method [36–38]. Low-order models (about 50 states) are obtained by truncating the data and considering only frequencies lower than 5 Hz. They are used for the control synthesis, while more accurate higher-order (about 200 states) models are used for simulation and validation.

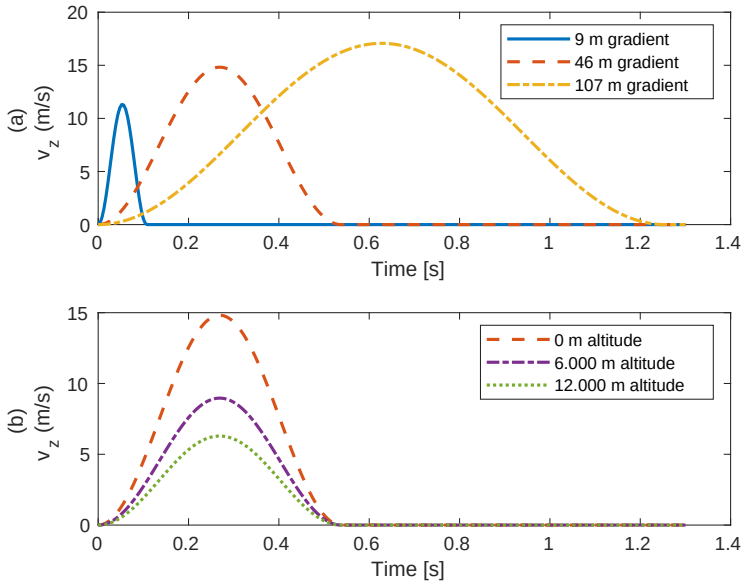

Fig. 1 Vertical wind velocity of discrete gust profiles of different gradient distances at 0 m altitude (a) and at different altitudes with a 46 m gradient distance (b)

B. Gust and Turbulence Models

The design of several parts of the aircraft is driven by the worst cases of winds, that can cause important loads on the structure. The wind not only has a static influence on the aircraft by applying static aerodynamic loads, but also has a dynamic influence resulting from the aeroelastic interaction between the structure and the unsteady aerodynamics. Two types of winds are generally considered in industry and literature:

- discrete gusts: short events of high wind velocity lasting at maximum a few tenths of seconds
- continuous turbulence: longer events of random wind velocity with less abrupt changes.

These two models correspond to the main cases described in official certification documents, such as the European CS-25 [39] that states the requirements for large aeroplanes. In particular, the article 25.341 provides a mathematical definition of discrete gusts and continuous turbulence that must be used for certification. The vertical discrete gust v_z is described in the time domain by the $1 - \cos$ expression:

$$v_z(t) = \begin{cases} \frac{U_{gust}}{2}\left[1 - \cos\left(\frac{\pi t V}{L_{gust}}\right)\right] & \text{if} \quad 0 \leq t \leq \frac{2L_{gust}}{V} \\ 0 \quad \text{otherwise} \end{cases} \tag{4}$$

where t is the time in s, V the TAS in m/s. L_{gust} is called the gradient distance in m and defines one half of the gust geometrical length. U_{gust} is the gust amplitude in m/s, which depends on L_{gust} and altitude. The range of gradient

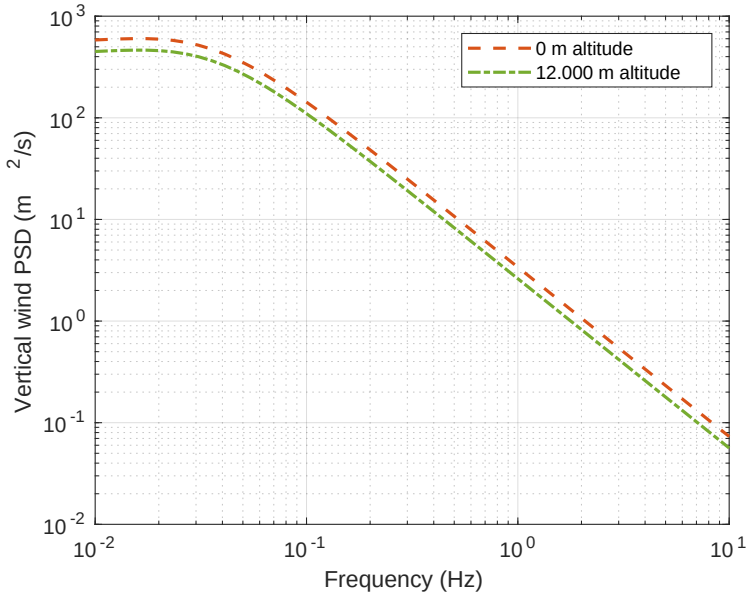

Fig. 2 Von Kármán turbulence profile of scale length 762 m at 0 m and 12.000 m

distances is generally comprised between 9 m and 107 m. In Fig. 1 time simulations of discrete gusts of various gradient distances (a) and at various altitudes (b) are shown for a TAS of 170 m/s. Short gusts have a lower amplitude but can excite higher frequency modes: due to the aircraft inertia and actuators limitations, they are more difficult to reject.

The continuous turbulence is a stochastic process, generally defined by its Power Spectral Density (PSD). In this work, the empirical von Kármán PSD for vertical turbulence [40] is used:

$$\Phi(\omega) = U_\sigma^2 \frac{L_{turb}}{\pi V} \frac{1 + \frac{8}{3}(1.339\frac{\omega L_{turb}}{V})^2}{[1 + (1.339\frac{\omega L_{turb}}{V})^2]^{11/6}} \tag{5}$$

where ω is the angular frequency in rad/s, L_{turb} is the scale of turbulence in m and U_σ is the turbulence standard deviation in m/s that diminishes with altitude. In Fig. 2 the von Kármán PSD is shown with a 762 m scale of turbulence, 170 m/s TAS and amplitudes computed at 0 m and 12.000 m using the equations defined in the European CS-25 [39].

C. Flight Domain

The need of restricting the range of velocity and height at which the aircraft can fly requires considering a simplified flight domain. The flight domain directly influences the controller design, as it prescribes the flight conditions at which the controller must be validated, as explained in more details in section III.A. In Fig. 3 the maximum altitude is 12.000 m and the maximum Mach number is 0.93. The iso-lines corresponding to five values of the Mach number are shown. Furthermore, in order to define the maximum velocity at which the aircraft can fly, the Calibrated Airspeed (CAS) is

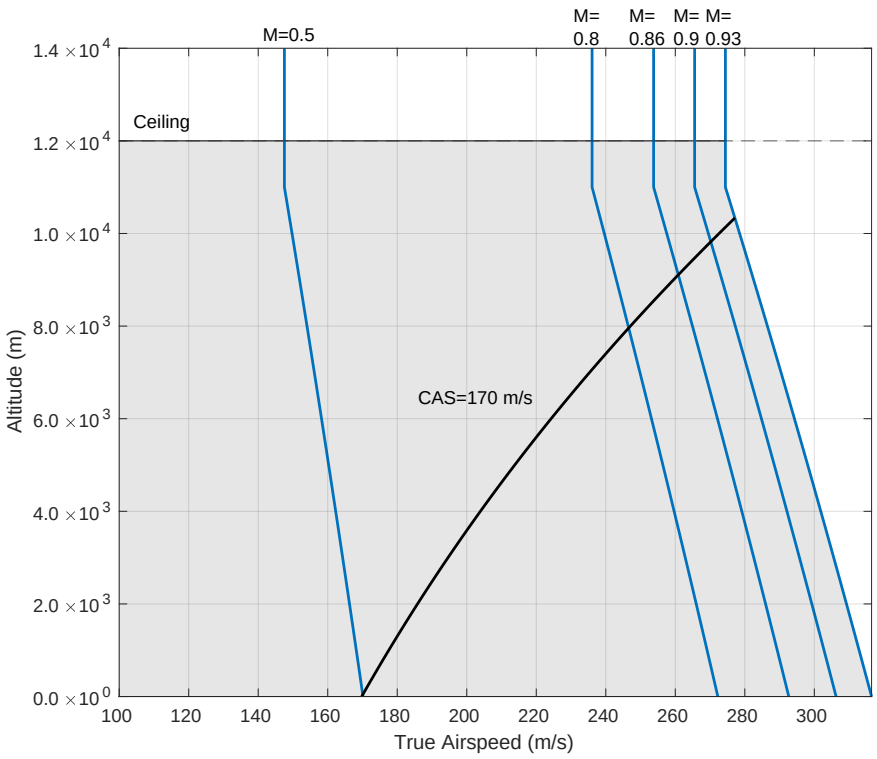

Fig. 3 Flight domain

used, and defined as:

$$CAS = a_0 \sqrt{5\left[\left(\frac{q_c}{P_0}+1\right)^{2/7}-1\right]} \tag{6}$$

where the impact pressure q_c is defined as

$$q_c = P\left[\left(1+0.2M^2\right)^{7/2}-1\right] \tag{7}$$

Here, a_0 is the speed of sound at 15°C, P_0 is the static pressure at sea level, and P is the local static pressure. In this work, the maximum velocity is fixed in terms of CAS at 170 m/s, and the corresponding iso-line is shown in Fig. 3. The maximum TAS hence depends on the Mach number (or equivalently on the altitude).

From the aeroelastic equation (1) it can be deduced that at a fixed Mach number, the dynamic pressure increases with the velocity and so do the aerodynamic forces and moments. Furthermore, at fixed Mach number, lower velocities correspond to higher altitudes, hence lower gust and turbulence amplitudes following the considerations made in section II.B. The external forces due to the wind decrease when the velocity decreases.

It is assumed for simplification that the maximum loads of the flight domain will be reached at maximum velocity. For these reasons, calculations will be performed only at the maximum speed defined by $CAS = 170$ m/s, assuming, and checking after, that the loads decrease at lower velocities. This follows a logic similar to the CS-25 certification [39],

where the loads are calculated at the cruise velocity called VC. The certification document also requires computations up to dive velocity (VD) with reduced Gust intensity. For this reason it is omitted in the present work. Following these considerations, the loads will be computed with models of various mass configurations and different values of Mach number, at fixed CAS. It is not straightforward which value of Mach number will lead to the higher loads: low values correspond to low TAS, as seen in Fig. 3, but at lower altitude, leading to higher wind amplitudes.

D. Sensors and Actuators Configuration

Several sensors are used for Gust Load Alleviation purposes. Gyroscopes and accelerometers provide reliable measurements of the pitch angle, pitch rate and the vertical acceleration of the aircraft which serve as basic information the controller can use to counteract the effects of gust onto the aircraft. In addition to those sensors, so-called alpha-probes provide a measurement of the angle of attack at the nose of the aircraft with a small phase advance. This measurement gives information of the wind perturbation and hence allows the controller to reduce the loads created in the wing structure.

The aircraft studied in this work is equipped with a lidar sensor that can remotely measure the wind velocity ahead of the aircraft. This is achieved [12] by a laser emitting light forward from the nose of the aircraft. The light is then scattered by air molecules through the quasi-static Rayleigh-Brillouin effect, and a sensor at the nose of the aircraft measures the frequency shift of the reflected light by Doppler effect and the wind velocity can be recovered. By emitting light in different directions (cone shape), the full velocity vector is obtained. The lidar allows the controller to act with phase advance with respect to the wind disturbance. The lidar provides measurement that are less reliable than those provided by the classical sensors, so high uncertainty and measurement noise must be used to model a lidar during the controller design.

The aircraft model used in this work includes twenty-three ailerons on each wing's trailing edge, a pair of elevators and a rudder. The elevators can turn the aircraft in the direction of the measured wind, hence reducing the relative vertical velocity and the loads they create. They are effective at low-frequency, as they require the whole aircraft pitch inertia to be solicited. The ailerons have a more direct effect, by creating local lift on the wing structure hence countering the acceleration created by the wind; they can control both low and high frequencies. The outermost ailerons create a higher lever arm, which helps reducing the wing bending moment, but the innermost ones have a more direct effect on the aircraft vertical load factor. It is not obvious which aileron position is more efficient, hence the interest of comparing different configurations. All actuators are limited by their maximum deflection angle and maximum deflection rate, the latter being generally more restraining that the former. The high frequency response of the aircraft is more difficult to control because of these limitations, and because of the high flexibility of the aircraft implying that the excitation of aeroelastic modes can create important loads at high frequency. The configuration with many ailerons allows to understand the most efficient locations for gust load alleviation, and the gain in performance and robustness

obtained by using several of them. By increasing the number of ailerons, the total surface of control is increased, giving more amplitude to the lift created to counter the gust loads.

III. Control strategy for Gust Load Alleviation

A. Objective: Gust Load Alleviation at multiple flight points and multiple mass configurations

In this section, the objective of this work are stated: we wish to find a single controller that minimizes the maximum loads on the aircraft structure due to the wind (defined by gusts and turbulence models of section II.B), based on multiple aeroelastic models defined in section II.A corresponding to different Mach number values and mass configurations.

It was shown in [29] that a GLA controller can reduce loads on different stations of the wing and at the Horizontal Tail Plane (HTP) simultaneously. In this work we focus on the bending moment (M_x) at the wing root, because of the important impact it has on the aircraft design, and, to a lesser extent, on the torsional moment (M_y) and the vertical shear force (T_z). The vertical load factor n_z, which is the vertical acceleration at the aircraft's center of gravity, is to be minimized too because of the effect it has on the passengers' and pilot's comfort. Note that when reducing the bending moment, the vertical shear force is reduced too because they are both the result of the integration of local vertical loads. On the contrary, as explained in II.D, an action of the ailerons to reduce the bending moment will generally lead to an increase of the torsional moment. Hence, a tradeoff is required between the two. With these objectives, only the longitudinal dynamics are to be considered for design and validation. The controller should also satisfy systems constraints, such as sensors and actuators limitations, and robustness constraints such as stability margins for each model considered.

B. General H_2/H_∞ framework

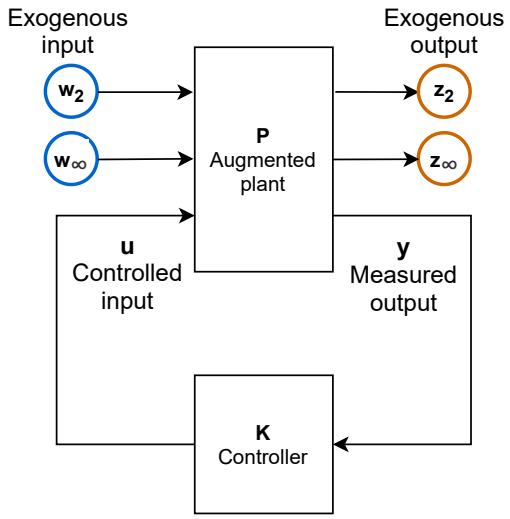

Fig. 4 General H_2/H_∞ formulation

The design of the laws for the control surfaces is based on the sensors and controllers described in section II.D. Their main objective is to minimize the aircraft loads while satisfying closed-loop stability and actuators, sensors and robustness constraints. This section describes the general framework used for H_2/H_∞ synthesis and analysis. This framework is common to the unstructured H_∞ synthesis, μ synthesis and structured H_∞ and H_2/H_∞ syntheses. The differences between these different methods will be highlighted in this section. Starting from the aeroelastic model of the aircraft described in section II.A, one can add additional filters and additional input/output ports to obtain an augmented system $P : \begin{pmatrix} \boldsymbol{w_\infty} \\ \boldsymbol{w_2} \\ \boldsymbol{u} \end{pmatrix} \mapsto \begin{pmatrix} \boldsymbol{z_\infty} \\ \boldsymbol{z_2} \\ \boldsymbol{y} \end{pmatrix}$. $\boldsymbol{u}$ and $\boldsymbol{y}$ are the controlled input and measured output respectively, while $\boldsymbol{w_\infty}$, $\boldsymbol{w_2}$, $\boldsymbol{z_\infty}$ and $\boldsymbol{z_2}$ are additional exogenous input/output. A visual representation of the augmented system is shown in Fig. 4. These additional filters and ports are chosen in such a way as to formulate the performance and constraints objectives as the minimization of the norms of the transfer functions [33]:

$$\left\| T_{\boldsymbol{w_\infty} \mapsto \boldsymbol{z_\infty}}(K) \right\|_\infty = \sup_\omega \bar{\sigma} \left(T_{\boldsymbol{w_\infty} \mapsto \boldsymbol{z_\infty}}(j\omega) \right) \tag{8}$$

$$\left\| T_{\boldsymbol{w_2} \mapsto \boldsymbol{z_2}}(K) \right\|_2 = \sqrt{\frac{1}{2\pi} \int_{-\infty}^{\infty} Tr \left(T_{\boldsymbol{w_2} \mapsto \boldsymbol{z_2}}(j\omega)^H T_{\boldsymbol{w_2} \mapsto \boldsymbol{z_2}}(j\omega) \right) d\omega} \tag{9}$$

where ω is the angular frequency, $\bar{\sigma}(A)$ is the maximum singular value of a generic matrix A, $Tr(A)$ its trace and A^H its transpose conjugate operator. The $T_{\boldsymbol{a} \mapsto \boldsymbol{b}}$ are the closed-loop transfer functions from generic quantity $\boldsymbol{a}$ to $\boldsymbol{b}$. The signals $\boldsymbol{w_\infty}$, $\boldsymbol{w_2}$, $\boldsymbol{z_\infty}$ and $\boldsymbol{z_2}$ do not necessarily correspond to physical quantities and the meaning of the H_∞ norm will depend on the choice of these variables. The H_∞ problem concerns the case where only the H_∞ norm is to be minimized. In case uncertainties are considered in the plant $\boldsymbol{P}$, the μ-synthesis applies [22]. If the controller is a general state-space model with order equal to that of $\boldsymbol{P}$, then the synthesis is referred to as unstructured, while if the controller exhibits a particular structure, such as a transfer function with some free parameters or a fixed-order state-space controller, then the synthesis is referred to as structured. Unstructured H_∞ and μ syntheses can take advantage of convex optimization [20–22], while structured syntheses rely on nonlinear methods [41].

C. Structured H_2/H_∞ synthesis with multiple models for Gust Load Alleviation

The augmented plant $\boldsymbol{P}$ used in this work is described in Fig. 5. The aeroelastic transfer functions $\boldsymbol{G^l}$ are those obtained from section II.A, while the wind is modeled as a 3-rd order rational approximation of the von Kármán turbulence treated as a transfer function:

$$\boldsymbol{H_v^l}(s) = U_\sigma^l \frac{0.02s^3 + 0.3398(L_{turb}/V)^2 s^2 + 2.7478(L_{turb}/V)s + 1}{0.1539(L_{turb}/V)^3 s^3 + 1.9754(L_{turb}/V)^2 s^2 + 2.9958(L_{turb}/V)s + 1} \tag{10}$$

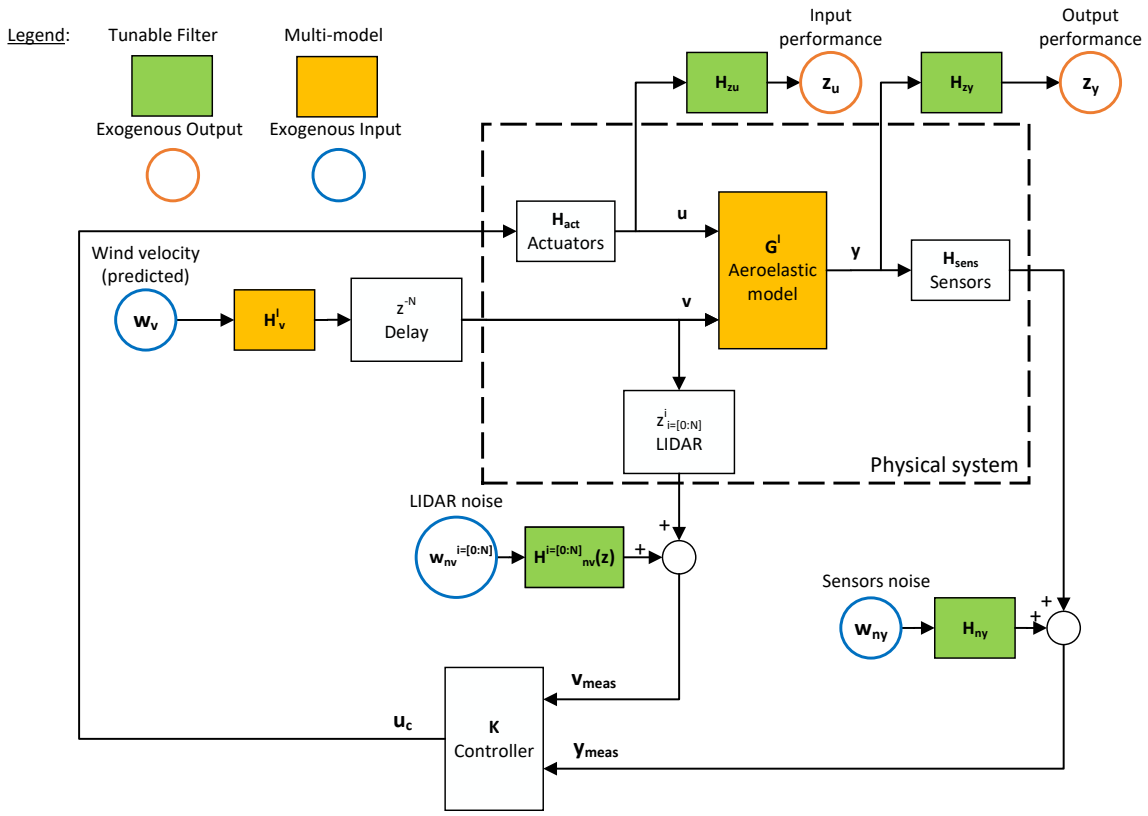

Fig. 5 Augmented system used for the H_2/H_∞ synthesis

where the same notations as in Eq. (5) have been used, and the turbulence intensity U_σ^l depends on the altitude of the l-th model. The lidar is defined as a tapped delay, keeping in memory all the values of the measured velocity ahead of the aircraft. Each point $i = [1 \dots N]$ corresponds to an intermediary distance between the aircraft nose and the maximum lidar measurement distance. The actuators are modeled as a second-order low-pass filter:

$$\boldsymbol{H_{act}}(s) = \frac{1}{s^2 + 2\xi\omega_0 s + \omega_0^2}\boldsymbol{I}_{N_u} \tag{11}$$

where $\boldsymbol{I}_{N_u}$ is the identity matrix of size N_u, the number of actuators, ω_0 and ξ are the actuators' cutoff frequency and damping ratio respectively. The sensors are represented by pure delays $\boldsymbol{H_{sens}} = z^{-\boldsymbol{\tau_{sens}}}$ where $\boldsymbol{\tau_{sens}}$ si a diagonal matrix with the value of the delay corresponding to each sensor on the diagonal. The $\boldsymbol{H_{zu}}$ filter defines the control surfaces maximum angle and angular rate constraints as:

$$\boldsymbol{H_{zu}}(s) = \begin{bmatrix} \frac{1}{u_{max}}\boldsymbol{I}_{N_u} \\ \frac{s}{\dot{u}_{max}(\epsilon s+1)}\boldsymbol{I}_{N_u} \end{bmatrix} \tag{12}$$

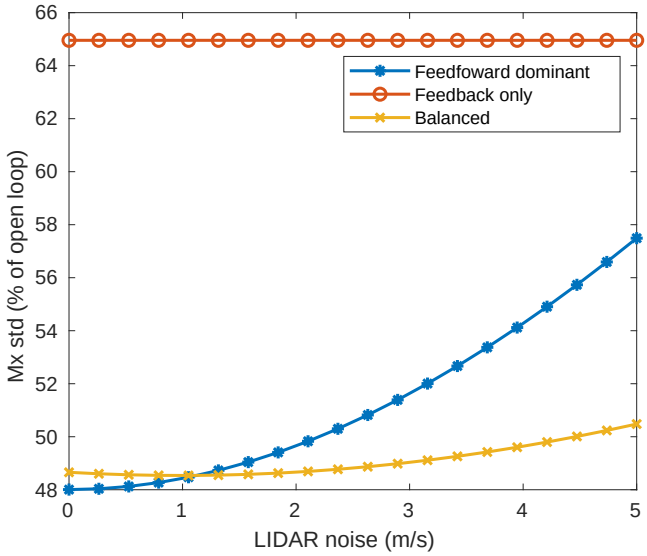

Fig. 6 Effect of the lidar noise on the GLA performance

where $\frac{s}{(\epsilon s+1)}$ is a pseudo derivative with $\epsilon \ll 1$, and u_{max} and $\dot{u}_{max}$ are the maximum deflection angle and deflection rate respectively. The GLA objective is defined through the filter $\boldsymbol{H_{zy}}$ as:

$$\boldsymbol{H_{zy}} = \text{diag}(\boldsymbol{\sigma_{ymax}})^{-1} \tag{13}$$

where $\boldsymbol{\sigma_{ymax}}$ is the maximum standard deviation of the outputs $\boldsymbol{y}$ that should be obtained with the worst considered turbulence. Finally, $\boldsymbol{H^i_{nv}}$ and $\boldsymbol{H_{ny}}$ are constant matrices defining the standard deviations of the lidar's and other sensors' measurement (white) noises respectively. More details of the choice of these filters can be found in [29].

As explained in section II.A, various aeroelastic models $\boldsymbol{G^l}$ are defined in this work, corresponding to different mass configurations and values of the Mach number. The models are indexed by the superscript ^{l}, that goes from 1 to 80 in the numerical applications. Similarly, one turbulence model $\boldsymbol{H^l_v}$ is used for each aeroelastic model, as the variation of velocity and altitude affects the amplitude and PSD of the wind following the considerations of sections II.B and II.C. It follows that the plant $\boldsymbol{P^l}$ defining the H_2/H_∞ problem is composed of different models. The controller synthesis used in this work is defined by the following optimization problem:

$$\min_K \max_l \left\| T^l_{w_2 \mapsto z_2}(K) \right\|_2 \tag{14}$$

$$\text{subject to} \tag{15}$$

$$\left\| T^l_{w_\infty \mapsto z_\infty}(K) \right\|_\infty \leq 1 \tag{16}$$

The transfer functions whose H_2 norm must be minimized are the transfer functions from disturbance and mea-

surement noise to the loads output, which are $T_{\boldsymbol{w_v} \mapsto z_y}$, $T_{\boldsymbol{w}^{\boldsymbol{i}}_{\boldsymbol{nv}} \mapsto z_y}$ and $T_{\boldsymbol{w_{ny}} \mapsto z_y}$. The H_∞ norm constraint imposes the maximum deflection angle and rate of the control surfaces to stay within the actuators acceptable bounds and is defined with the $T_{\boldsymbol{w_v} \mapsto z_u}$ transfer function. Furthermore, robustness margins constraints are imposed through the H_∞ norm of a transfer function based on the sensitivity function [41]. The H_2 criterion is more efficient for optimal performance, as it works on the whole frequency range, while the H_∞ focuses on the one frequency at which the transfer function gain is maximum. An extreme example is the case where there exists a high frequency peak in the system's response, which the controller cannot attenuate due to its limitations. In this case, the closed-loop H_∞ norm will be calculated on this peak, and the response at the other frequencies will be ignored, leading to an inefficient controller. Some tuning of the shape filters would be required to ignore the peak in the synthesis, which would increase the system's order and require fine tuning of each model independently. The H_2 criterion is computed on the whole frequency range, and not only on the peak response, hence requires no extra tuning. However, the H_∞ norm provides strong guarantees such as stability, robustness and satisfaction of system's limitations. The mixed H_2/H_∞ synthesis hence provides a good performance while ensuring guarantees in worst case scenarios when required.

The controller $\boldsymbol{K}$ in Eq. (14) has a fixed structure, composed of two state-space models: one for the feedforward part that takes the lidar measurement as input, and one for the feedback part that takes the pitch rate, vertical load factor and angle-of-attack as input. In order to reduce the controller's sensitivity to lidar noise or to a failure, one can increase the gain of the $\boldsymbol{H}^{\boldsymbol{i}}_{\boldsymbol{nv}}$ filter in Fig. 5. However, we find it more efficient and straightforward to perform two syntheses: a first synthesis calculates the feedback controller without the feedforward part, then the latter is obtained from a synthesis based on the obtained closed-loop. This is illustrated by Fig. 6 where the M_x alleviation of a controller obtained without separating the feedback and feedforward parts is compared to that of a pure feedback controller (hence not depending on the lidar noise) and of a controller obtained with the procedure defined before. It can be seen that the balanced controller is less sensitive to the lidar noise. The ratio between the importance of the classical sensors and that of the lidar in the controller response can be adjusted by tuning the maximum actuator's angle and rate during the feedback synthesis.

Note that the synthesis problem described above cannot be solved by convex optimization. The structured H_2/H_∞ problem with multiple models described above can be directly implemented within Matlab's *systune* function, based on the work described in [41].

IV. Results: Gust Load Attenuation at various flight points and mass configurations with a single robust controller

A. Description of the Simulations Configuration and Parameters

The results exposed in this section are obtained from simulations performed with Matlab and Simulink. They are based on controllers synthesized by Matlab's *systune* function, following techniques described in section III. The

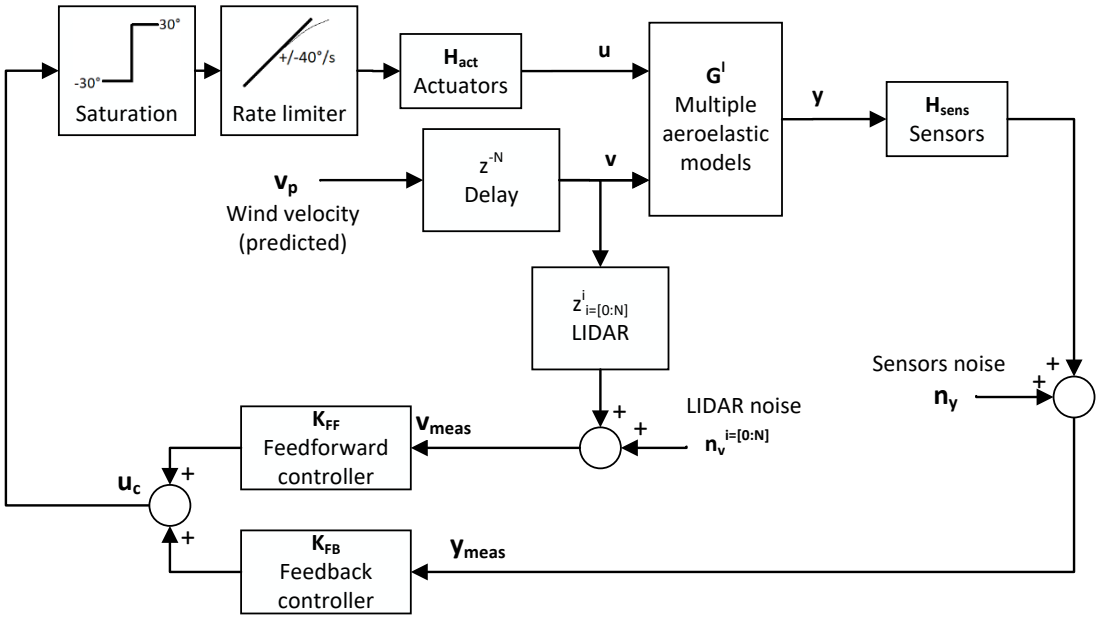

Fig. 7 System used for simulations

configuration used for simulations is shown in Fig. 7 and is slightly different from the one used during design. The first difference lies in the aeroelastic state-space models, which are of high order for simulations (about 200-th order) to improve the accuracy, while reduced-order models (about 50-th order) are used for the controllers design in order to obtain an acceptable computational cost. Furthermore, while the design configuration of Fig. 5 relies on a linear model, a saturation and rate limiter are applied to the controlled variables, in order to impose the ailerons and elevators angles to satisfy the maximum angle and angular rate constraints imposed by the system. Finally, the tuning filters used for shaping the H_2/H_∞ criteria are removed in the simulations configuration and replaced with physical values.

The simulations are performed with the wind models described in section II.B, and contrarily to the design phase, turbulence time series based on the true von Kármán PSD are generated. The lidar noise at intermediary measurement point i is defined as $n_v^i = \sigma_v w_0$ and the other sensors' noise is defined as $\boldsymbol{n_y} = \boldsymbol{\sigma_y w_y}$ where the w_0 and $\boldsymbol{w_y}$ are unit variance white noises. Note that with this definition, we assume that the intermediary lidar measurements come from a single measurement that has been delayed, and not from independent sources. The difference between the two possible configurations is studied in [29]. The actuators and sensors models are the same as those used for design and described in section III.C. The values of the parameters used in simulations and design are gathered in table 2. The different values of the Mach number are included, and the corresponding TAS, CAS and altitude can be deduced from the considerations of section II.C. Gusts corresponding to gradient distances lower than 107 m lead to loads that are more difficult to

Quantity	Symbol	Value
Mach number values	M	0.5, 0.8, 0.86, 0.9, 0.93
Number of mass configurations	–	16
Actuators cutoff frequency	ω_0	4 Hz
Actuators damping ratio	ξ	0.85
Maximum deflection angle	u_{max}	30°
Maximum deflection rate	$\dot{u}_{max}$	40 °/s
Sensors delays	$\boldsymbol{\tau_{sens}}$	40 ms for each sensor
Sensors noise amplitude	$\boldsymbol{\sigma_y}$	0
Lidar noise amplitude	σ_v	$0.04V$
Discrete gusts gradient	L_{gust}	107 m
Scale of turbulence	L_{turb}	762 m
Time step	T_s	0.02 s

Table 2 Numerical values used in simulations

attenuate, but that are also lower because of the lower corresponding wind amplitudes. For this reason and for the sake of conciseness, only the results of the 107 m gust are shown. Also note that the classical sensors' noise is assumed negligible in comparison to the lidar noise, and therefore is simply set to zero.

B. Results

In this section, different controllers are synthesized using the methodology and parameters exposed above. As stated in section III.A, we focus on the alleviation of the bending moment M_x at the wing root and the vertical load factor n_z at the center of gravity of the aircraft. The torsional moment M_y at wing root and the vertical shear force T_z at wing root are of secondary importance, and a small increase can be acceptable. In particular, the maximum loads calculated on 80 different models of various mass configuration and value of Mach number are to be minimized. Recall from section II.D that the model included 23 ailerons on each wing. Several configurations of these ailerons are studied. Note that the computed loads are dynamical increments with respect to an equilibrium, they must be added to the statical loads (mainly due to the lift, drag and weight) to obtain the total loads.

1. Time simulations with a single model

Time simulations have been performed with a robust controller that uses two ailerons of large size on each wing (16 ailerons assembled into two groups), corresponding to about two thirds of each wing. The aeroelastic model is obtained with a Mach number of 0.86 and an empty aircraft configuration. In this case, the minimization of all the outputs of interest has been included in the performance objective of the H_2/H_∞ synthesis. In Fig. 8, the wind velocities (a) during a positive 107 m gust and during a von Kármán turbulence are shown. The time response of the aircraft aeroelastic dynamics to these wind disturbances is represented too, through the load factor and wing root loads of interest. Note

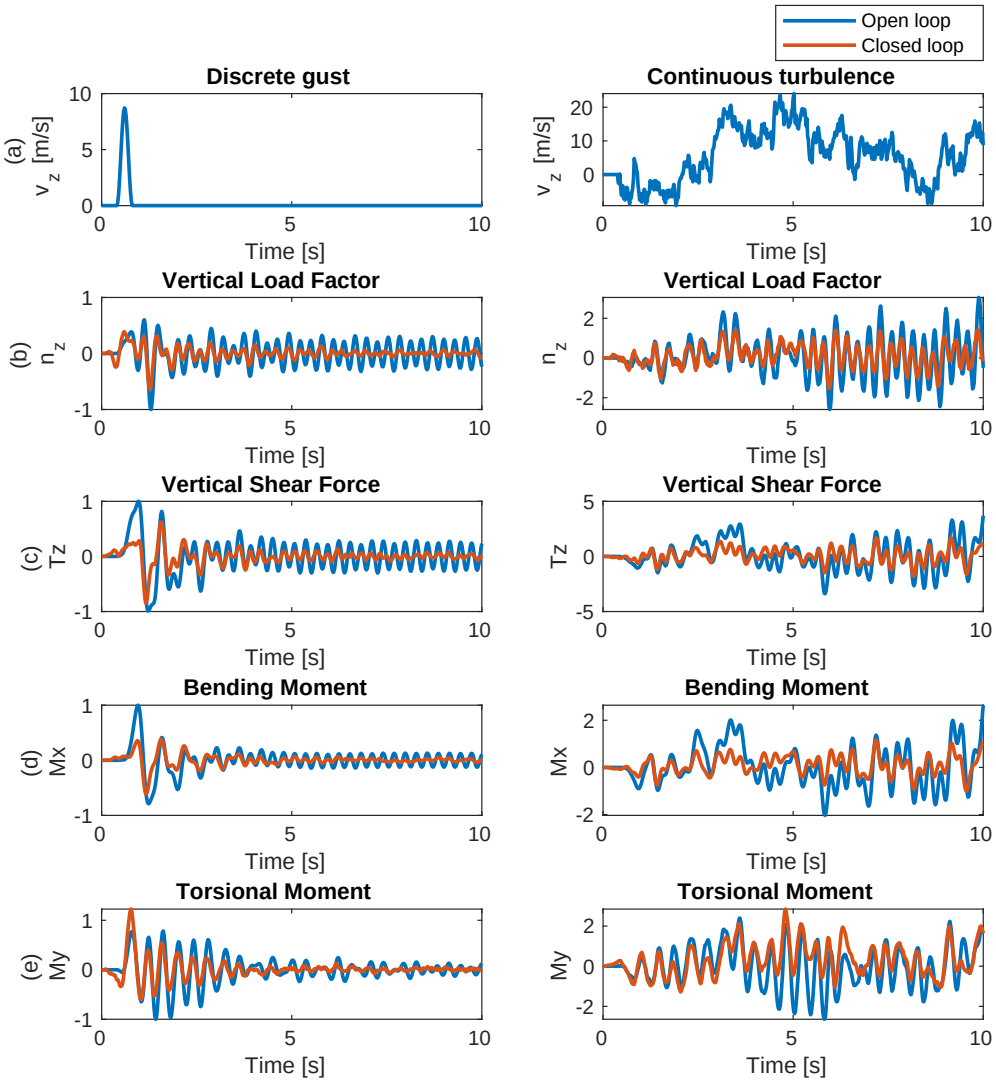

Fig. 8 Wind velocity and outputs of interest (normalized) from time simulations with discrete gust and von Kármán Turbulence (empty aircraft, M=0.86, two groups of eight ailerons on each wing)

that the outputs are normalized for intellectual property issues. It can be seen that the controller successfully attenuates an oscillatory mode of about 4 Hz frequency. Moreover, the maximum absolute value of the bending moment (d) and of the vertical load factor (b) are reduced by about one third with respect to the open loop in the discrete gust response, and the standard deviation is divided by a factor of two in the turbulence response. Finally, the vertical shear force (c) is slightly attenuated, while the torsional moment (e) tends to increase due to the controller action. In Fig. 9, the corresponding control surfaces' deflection angle and rate are shown. It can be seen that thanks to the lidar measurements, the controller can start before the discrete gust has arrived. The deflection angle stay within a $[-7°, 7°]$ range, far from the saturation limit. This information is of particular importance, as it also means that the linear approximation for the control surface action onto the aircraft response is valid. The deflection rate (b) is close to saturation during the

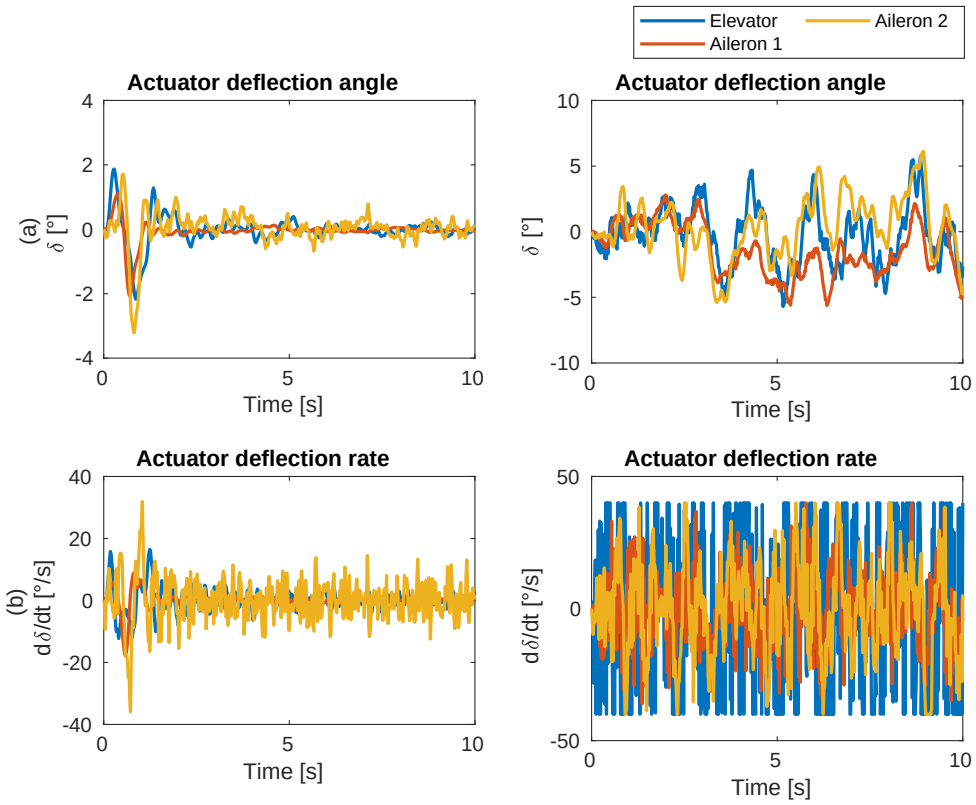

Fig. 9 Control surfaces angle deflection and angular rate from time simulations with discrete gust and von Kármán Turbulence (empty aircraft, M=0.86, two groups of eight ailerons on each wing)

discrete gust, and the limits are reached in the turbulence simulations. Note that due to the low amount of time spent in saturated mode, the performance is only slightly affected. The noisy actuator response when steady-state has been reached after the discrete gust is due to the lidar noise.

2. Comparison of the loads envelopes with one robust controllers and with different local controllers

The time simulations shown above are obtained with a single model, we now perform similar simulations on different models in order to study the maximum loads in the flight envelope. In Fig. 10, the correlated loads obtained by simulations with the 80 aeroelastic models and with the same multi-model robust controller used in Fig. 8 and 9 are shown (blue points) and compared to the case without controller (green points). For a pair of outputs, each point corresponds to the minimum or maximum of one of the two outputs, defining one coordinate, and the other coordinate is computed as the value of the other output at the time this minimum/maximum has been obtained. Both positive and negative discrete gusts are used, resulting in eight times as many points as different models. In the case of turbulence, only one simulation is performed at each point, leading to four times as many points as models. In addition to proving a practical representation of the maximum loads, the correlated loads are useful in the case of the M_x/M_y pair for stress analysis, whether the maximum bending and torsional moments occur simultaneously or not can lead to different

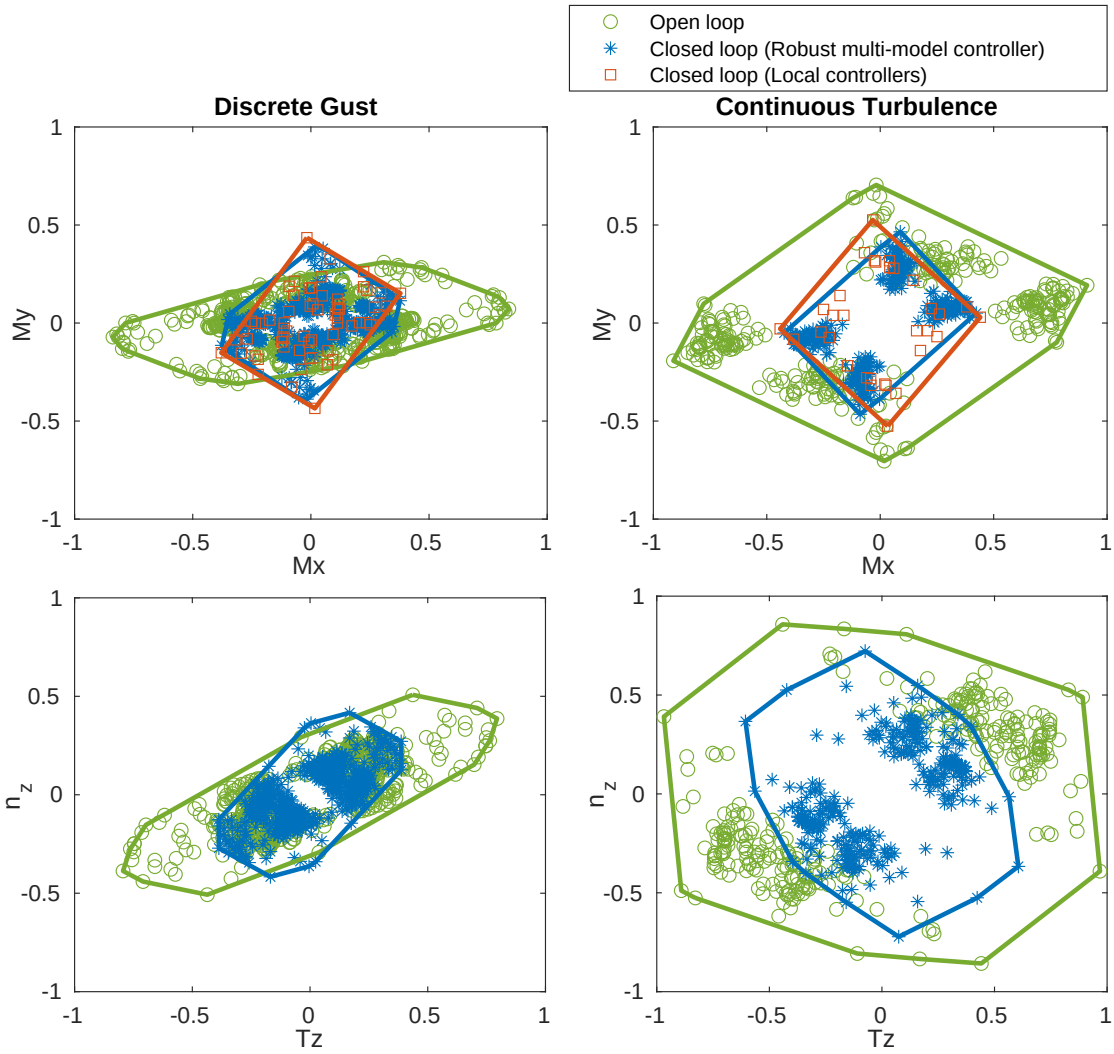

Fig. 10 Correlated bending/torsional moments and shear force/load factor with 80 models of various mass configuration and Mach number values. Comparison of a robust controller designed with multiple models, and local controllers designed for each model

impacts on the structure. The outputs are normalized with common coefficients, allowing to appreciate the relative values of the different configurations. The comparison between the closed loop obtained with the multi-model robust controller and the open loop shows the capability of a single low-order controller to divide the maximum wing root bending moment M_x by a factor of 2 both for discrete gust and turbulence. A reduction of the maximum vertical load n_z factor by about 30% is also obtained. The shear force T_z, as expected, follows the trend of the bending moment and is alleviated too. However, the maximum torsional moment M_y is not reduced, it is even increased with respect to the open loop case. This observation will be discussed below. Finally, the Fig. 10 also shows the comparison of the multi-model robust controller with local controllers, represented by the red points. One controller has been designed for each model defining the external load envelope of the pair M_x/M_y obtained with the multi-model robust controller. The reason

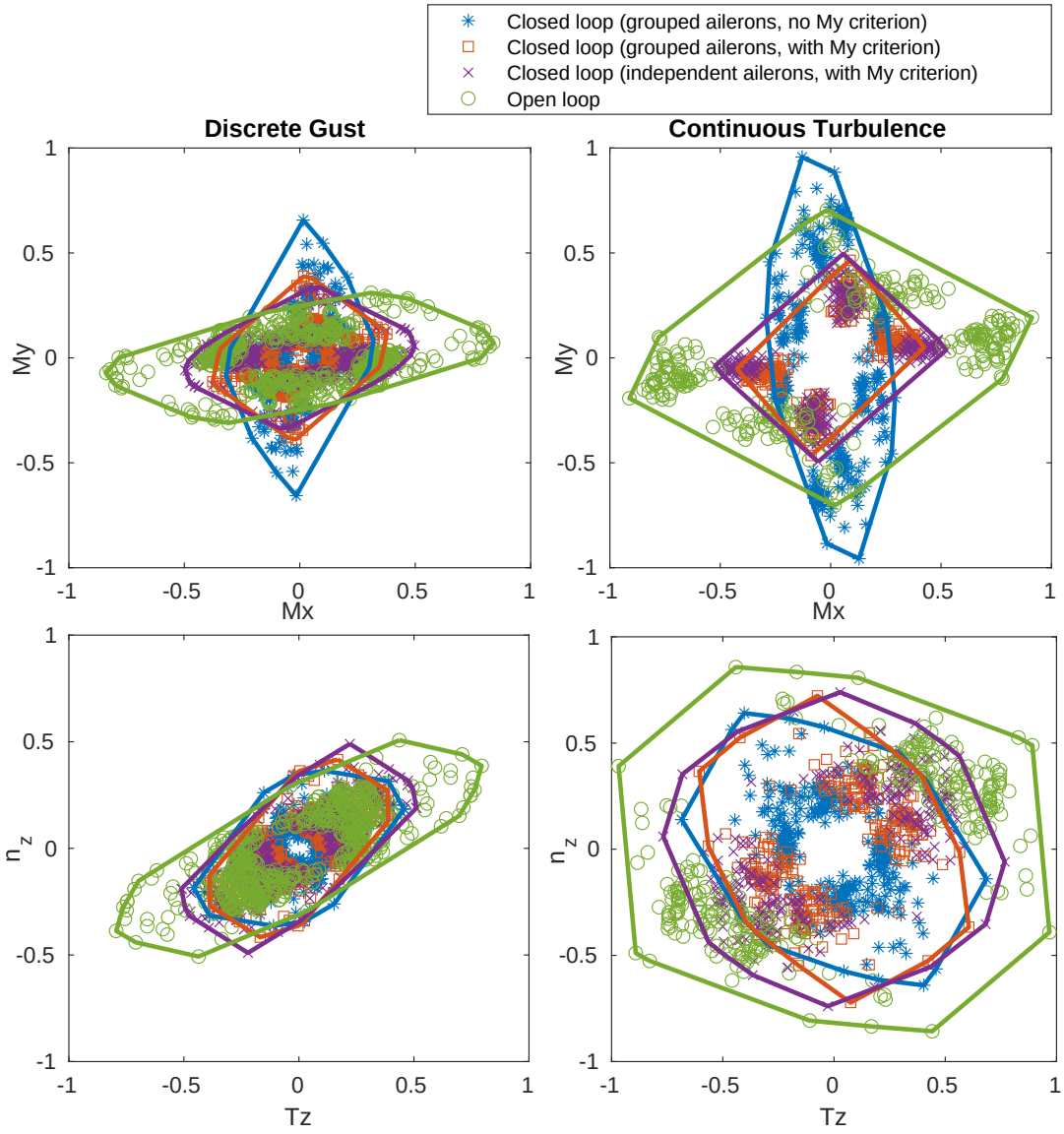

Fig. 11 Correlated bending/torsional moments and shear force/load factor with 80 models of various mass configuration and Mach number values with and without a torsion moment attenuation criterion in the controller design, with grouped or independent ailerons.

for not designing one controller for each of the 80 models is that verifying that each synthesis has been performed correctly can become tedious. It can be seen that the difference between the multi-model robust controller and the local controllers is very low. Note that the controller designed with various models naturally acquires robustness, while in the case of local controllers, additional constraints must be imposed during the design to obtain a comparable level of robustness. This explains why the multi-model robust controller can even slightly outperform the local controllers sometimes. As the local controllers are obtained with models that define a M_x/M_y envelope, showing their results on the T_z/n_z envelope would be meaningless.

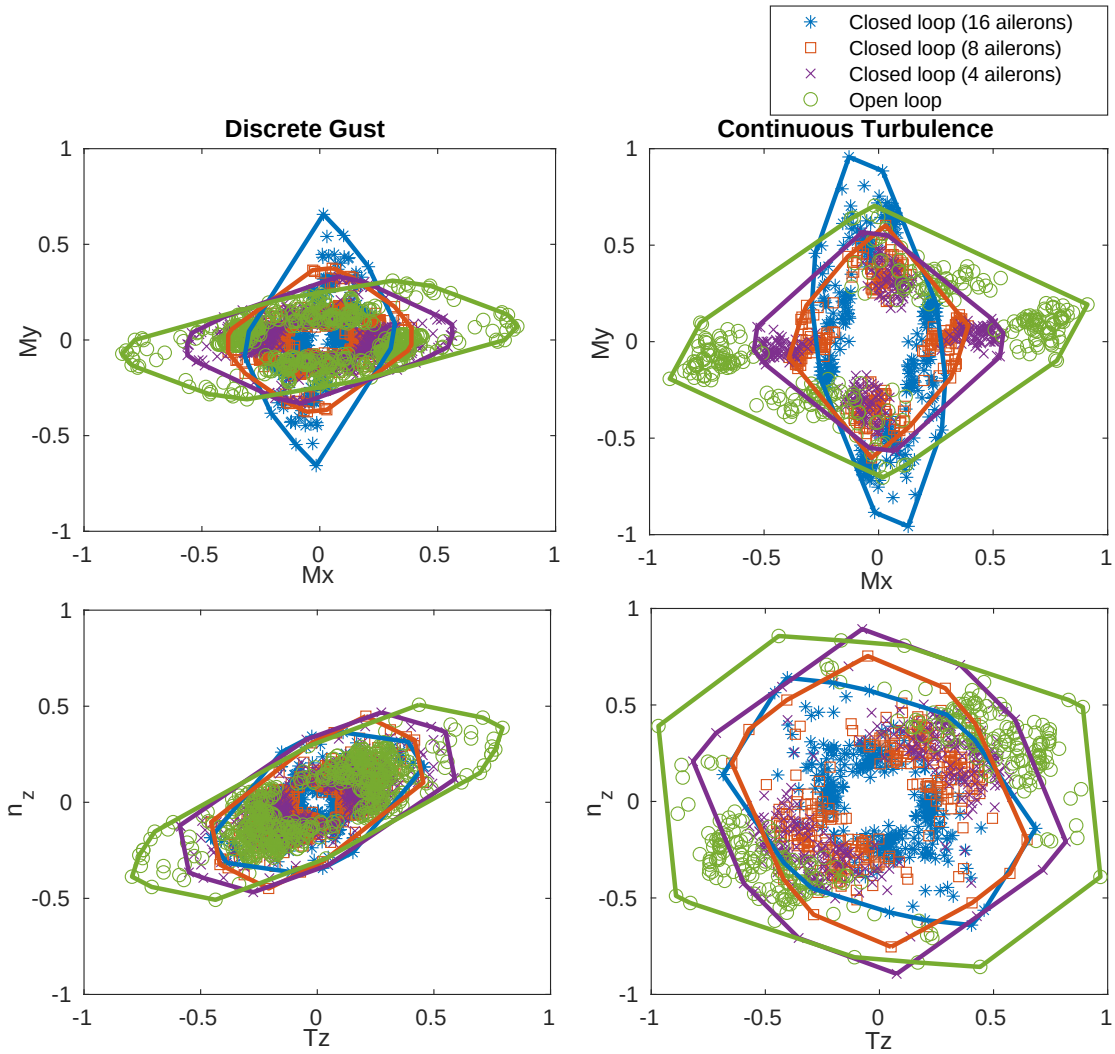

Fig. 12 Correlated bending/torsional moments and shear force/load factor with 80 models of various mass configuration and Mach number values, for different ailerons size, defined by the number of small ailerons grouped together

3. Influence of the performance criterion on the multiple loads alleviation capability

The results shown before have been obtained with a controller that uses two ailerons of large size on each wing, designed to minimize simultaneously all the outputs of interest (M_x, n_z, M_y and T_z). One can now wonder whether the bending moment could be further attenuated, possibly at the expense of the other outputs that are of lesser importance for the aircraft design. In Fig. 11, the same configuration as Fig. 8 9 10 is shown in red and compared to the case where the torsional moment reduction objective is dropped (blue points). In the latter case, the maximum bending moment is strongly reduced, leading to a 70% reduction with respect to the open loop for the turbulence case against 50% when the M_y criterion is used. The torsional moment is increased by 30% when the M_y criterion is not used, while it is attenuated by the same amount otherwise. The n_z and T_z are only slightly affected by this change. Furthermore, the purple points

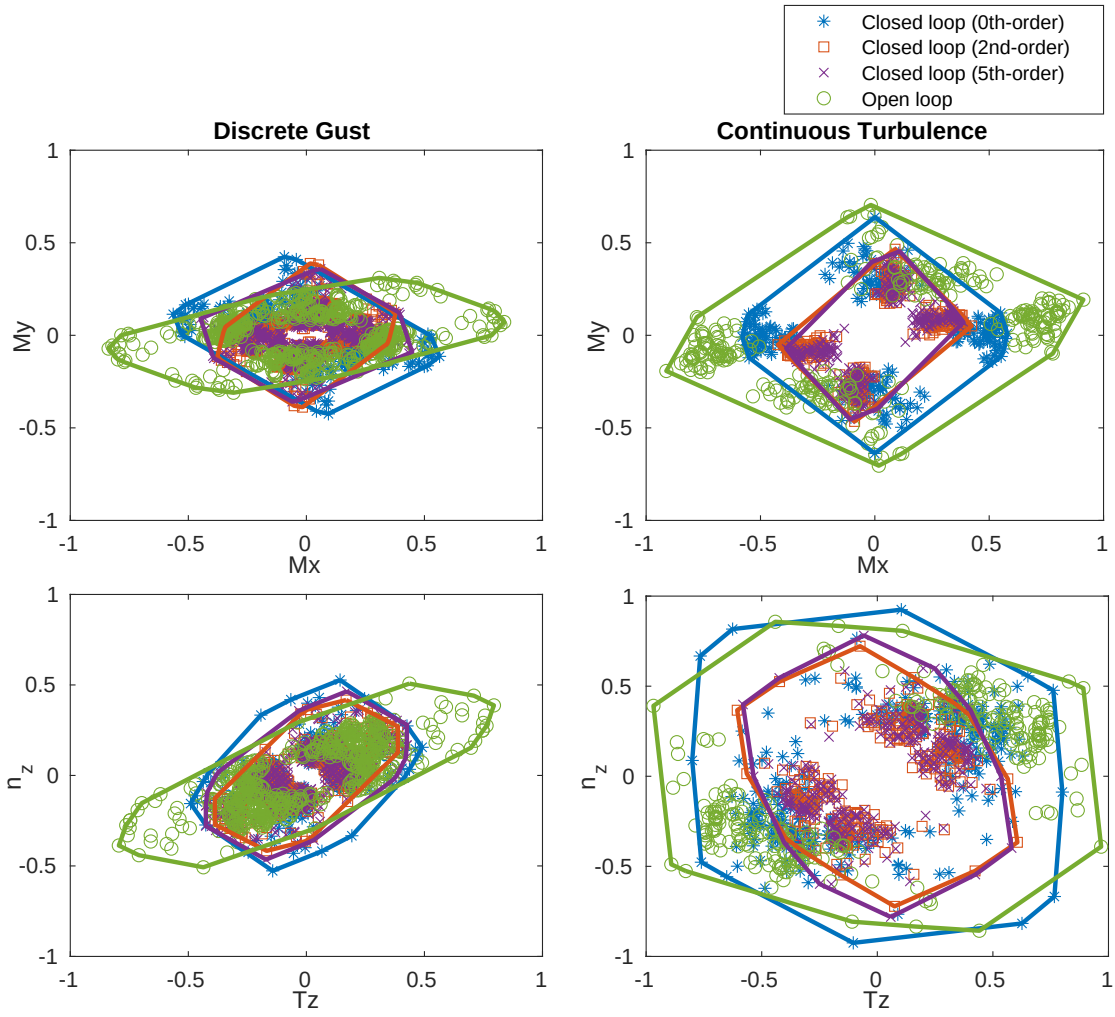

Fig. 13 Correlated bending/torsional moments and shear force/load factor with 80 models of various mass configuration and Mach number values, for different controller's order

show the case where the two groups of large ailerons are split into independent smaller ailerons, and the M_y criterion is included. By keeping the total control surface size constant and separating the ailerons, hence increasing the number of degrees of freedom, the objective is to improve the output controllability of the system and better attenuate the different loads simultaneously. It can be seen in the figure that this is not the case, the slight reduction of the maximum torsional moment with the discrete gust with respect to the case in which the ailerons are grouped is at the expense of an increase of the bending moment.

4. Influence of the ailerons size on the loads envelopes

In Fig. 12, correlated loads computed with various ailerons sizes are shown. The M_y criterion has been dropped in this case. Note that the ailerons are assembled into two groups, hence the size of each group is determined by the number of ailerons. It can be seen that a reduction of the ailerons size leads to a reduced bending moment and vertical

load factor alleviation capability, and to a lower maximum torsional moment. These results, together with those of Fig. 11, show that it is difficult to reduce significantly the bending moment and the torsional moment at the same time. When an increase of the torsional moment is acceptable, increasing the ailerons size leads to improved bending moment and load factor attenuations.

5. Influence of the controller order on the loads envelopes

Finally, the choice of using 2nd-order controllers is put to the test. In Fig. 13, controllers of order 0 (static gain), 2 and 5 are compared. It can be clearly seen that the order 2 brings a significant improvement with respect to the static gain, while increasing the order further does not lead to better performance.

V. Conclusion

This work aims to understand whether a single robust controller can be used to reduce the maximum loads and load factors that can occur during an aircraft life, and if so, what is the influence of the ailerons configuration and the controller order. After a definition of the aeroelastic and wind models in line with the international certification procedures, a multi-model H_2/H_∞ synthesis strategy is proposed to obtain low-order controllers that can be easily implemented in commercial aircraft's onboard computers, and which take advantage of different sensors including a lidar to minimize the loads in presence of robustness and system constraints. Time simulations based on such controllers and multi-point validation models are performed, and the influence of the ailerons configuration, the controller's order and the performance criteria onto the multi-load alleviation capability is assessed.

It results from the simulations that the proposed H_2/H_∞ synthesis leads to controllers that can reduce the bending moment and vertical load factor up to 50% on a single aeroelastic model, even in presence of saturation limits. The multi-model robust approach does not suffer from any loss of performance compared to a case where one controller has been designed at each flight point and mass configuration. This means that a perfectly adaptive controller based on the same structure as in this work and with the same system and robustness constraints would not improve the load alleviation performance. Furthermore, the angle deflection constraint in never approached, the angles staying within the $[-7°, 7°]$ range, while the deflection rate limit is reached. This means that the linear hypothesis concerning the control surfaces' action is valid in this work, and that increasing the angular velocity limits of the actuators would probably improve the performance, as long as the nonlinear effects are not too significant. The results also show that reducing the bending and torsional moments simultaneously is difficult, and an augmentation of the latter is generally needed when higher attenuations of the former are sought. This is particularly visible when the ailerons' size increases, and with ailerons that occupy about two third of the wing's trailing edge, a 70% alleviation of the maximum bending moment and a 30% reduction of the maximum vertical load factor, at the expense of a 30% increase of the maximum torsional moment. Finally, it is shown that using a second-order structured controller significantly improves the loads alleviation

with respect to a static gain, and going above 2 is useless. This conclusion is valid within the low-order structured controller framework described in this work. Indeed, it was shown in [29] that unstructured controllers of very high order could be more efficient than reduced-order ones.

The only point of comparison available in this work is the case where one controller is designed for flight points and mass configuration. Performing a formal comparison between the robust approach and MPC strategies in similar conditions and studying their robustness capabilities would help understand the true gain in performance that can be achieved with nonlinear control. Likewise, a formal comparison with an adaptive strategy using a lidar would help identify the loss of performance when using a single fixed controller.

References

[1] Moulin, B., and Karpel, M., "Gust Loads Alleviation Using Special Control Surfaces," *Journal of Aircraft*, Vol. 44, No. 1, 2007, pp. 17–25. https://doi.org/10.2514/1.19876.

[2] Fonte, F., Ricci, S., and Mantegazza, P., "Gust Load Alleviation for a Regional Aircraft Through a Static Output Feedback," *Journal of Aircraft*, Vol. 52, No. 5, 2015, pp. 1559–1574. https://doi.org/10.2514/1.c032995.

[3] Che, J., Gregory, I., and Cao, C., "Integrated Flight/Structural Mode Control for Very Flexible Aircraft Using L1 Adaptive Output Feedback Controller," *AIAA Guidance, Navigation, and Control Conference*, American Institute of Aeronautics and Astronautics, 2012. https://doi.org/10.2514/6.2012-4439.

[4] Stanford, B., "Gradient-Based Aeroservoelastic Optimization with Static Output Feedback," *AIAA Scitech 2019 Forum*, American Institute of Aeronautics and Astronautics, 2019. https://doi.org/10.2514/6.2019-0216.

[5] Mokrani, B., Palazzo, F., Mottershead, J. E., and Fichera, S., "Multiple-Input Multiple-Output Experimental Aeroelastic Control Using a Receptance-Based Method," *AIAA Journal*, Vol. 57, No. 7, 2019, pp. 3066–3077. https://doi.org/10.2514/1.J057855, URL https://doi.org/10.2514/1.J057855.

[6] Alam, M., Hromcik, M., and Hanis, T., "Active gust load alleviation system for flexible aircraft: Mixed feedforward/feedback approach," *Aerospace Science and Technology*, Vol. 41, 2015, pp. 122–133. https://doi.org/10.1016/j.ast.2014.12.020.

[7] Wildschek, A., Stroscher, F., Klimmek, T., Šika, Z., Vampola, T., Valášek, M., Gangsaas, D., Aversa, N., and Berard, A., "Gust Load Alleviation on a Large Blended Wing Body Airliner," *27th International Congress of the Aeronautical Sciences*, 2010.

[8] Magar, K. S. T., Reich, G. W., Pankonien, A. M., and Smyers, B., "Active Gust Alleviation using Artificial Hair Sensors and Feedforward Control," *AIAA Guidance, Navigation, and Control Conference*, American Institute of Aeronautics and Astronautics, 2017. https://doi.org/10.2514/6.2017-1485.

[9] Zhao, Y., Yue, C., and Hu, H., "Gust Load Alleviation on a Large Transport Airplane," *Journal of Aircraft*, Vol. 53, No. 6, 2016, pp. 1932–1946. https://doi.org/10.2514/1.c033713.

[10] Li, F., Wang, Y., and Ronch, A. D., "Flight Testing an Adaptive Feedforward Controller for Gust Loads Alleviation on a Flexible Aircraft," *AIAA Atmospheric Flight Mechanics Conference*, American Institute of Aeronautics and Astronautics, 2016. https://doi.org/10.2514/6.2016-3100.

[11] Wildschek, A., Maier, R., Hoffmann, F., Jeanneau, M., and Baier, H., "Active Wing Load Alleviation with an Adaptive Feed-forward Control Algorithm," *AIAA Guidance, Navigation, and Control Conference and Exhibit*, American Institute of Aeronautics and Astronautics, 2006. https://doi.org/10.2514/6.2006-6054.

[12] Herbst, J., and Vrancken, P., "Design of a monolithic Michelson interferometer for fringe imaging in a near-field, UV, direct-detection Doppler wind lidar," *Applied Optics*, Vol. 55, No. 25, 2016, p. 6910. https://doi.org/10.1364/ao.55.006910.

[13] Rabadan, G. J., Schmitt, N. P., Pistner, T., and Rehm, W., "Airborne Lidar for Automatic Feedforward Control of Turbulent In-Flight Phenomena," *Journal of Aircraft*, Vol. 47, No. 2, 2010, pp. 392–403. https://doi.org/10.2514/1.44950.

[14] Haghighat, S., Liu, H. H. T., and Martins, J. R. R. A., "Model-Predictive Gust Load Alleviation Controller for a Highly Flexible Aircraft," *Journal of Guidance, Control, and Dynamics*, Vol. 35, No. 6, 2012, pp. 1751–1766. https://doi.org/10.2514/1.57013.

[15] Giesseler, H.-G., Kopf, M., Varutti, P., Faulwasser, T., and Findeisen, R., "Model Predictive Control for Gust Load Alleviation," *IFAC Proceedings Volumes*, Vol. 45, No. 17, 2012, pp. 27–32. https://doi.org/10.3182/20120823-5-nl-3013.00049.

[16] d. Virgilio Pereira, M., Kolmanovsky, I., Cesnik, C. E., and Vetrano, F., "Model Predictive Control Architectures for Maneuver Load Alleviation in Very Flexible Aircraft," *AIAA Scitech 2019 Forum*, American Institute of Aeronautics and Astronautics, 2019. https://doi.org/10.2514/6.2019-1591.

[17] Gaulocher, S. L., Roos, C., and Cumer, C., "Aircraft Load Alleviation During Maneuvers Using Optimal Control Surface Combinations," *Journal of Guidance, Control, and Dynamics*, Vol. 30, No. 2, 2007, pp. 591–600. https://doi.org/10.2514/1.25577.

[18] Fezans, N., and Joos, H.-D., "Combined Feedback and LIDAR-Based Feedforward Active Load Alleviation," *AIAA Atmospheric Flight Mechanics Conference*, American Institute of Aeronautics and Astronautics, 2017. https://doi.org/10.2514/6.2017-3548.

[19] Fezans, N., Schwithal, J., and Fischenberg, D., "In-flight remote sensing and identification of gusts, turbulence, and wake vortices using a Doppler LIDAR," *CEAS Aeronautical Journal*, Vol. 8, No. 2, 2017, pp. 313–333. https://doi.org/10.1007/s13272-017-0240-9.

[20] Doyle, J., A, F., and Tannenbaum, A., *Feedback Control Theory*, Macmillan Publishing Co., 2009, pp. 45–59. https://doi.org/10.1007/978-0-387-85460-1_1.

[21] Skogestad, S., *Multivariable feedback control : analysis and design*, Wiley, Chichester New York, 1996, pp. 40–62.

[22] Vidyasagar, M., and Kimura, H., "Robust controllers for uncertain linear multivariable systems," *Automatica*, Vol. 22, No. 1, 1986, pp. 85 – 94. https://doi.org/https://doi.org/10.1016/0005-1098(86)90107-X, URL http://www.sciencedirect.com/science/article/pii/000510988690107X.

[23] Zeng, J., Kukreja, S. L., and Moulin, B., "Experimental Model-Based Aeroelastic Control for Flutter Suppression and Gust-Load Alleviation," *Journal of Guidance, Control, and Dynamics*, Vol. 35, No. 5, 2012, pp. 1377–1390. https://doi.org/10.2514/1.56790.

[24] Cook, R. G., Palacios, R., and Goulart, P., "Robust Gust Alleviation and Stabilization of Very Flexible Aircraft," *AIAA Journal*, Vol. 51, No. 2, 2013, pp. 330–340. https://doi.org/10.2514/1.J051697, URL https://doi.org/10.2514/1.J051697.

[25] Ferrier, Y., Nguyen, N. T., Ting, E., Chaparro, D., Wang, X., de Visser, C. C., and Chu, Q. P., "Active Gust Load Alleviation of High-Aspect Ratio Flexible Wing Aircraft," *2018 AIAA Guidance, Navigation, and Control Conference*, American Institute of Aeronautics and Astronautics, 2018. https://doi.org/10.2514/6.2018-0620.

[26] Waitman, S., and Marcos, A., "H-infinity Control Design for Active Flutter Suppression of Flexible-Wing Unmanned Aerial Vehicle Demonstrator," *Journal of Guidance, Control, and Dynamics*, Vol. 43, No. 4, 2020, pp. 656–672. https://doi.org/10.2514/1.G004618, URL https://doi.org/10.2514/1.G004618.

[27] Pusch, M., Ossmann, D., and Luspay, T., "Structured Control Design for a Highly Flexible Flutter Demonstrator," *Aerospace*, Vol. 6, No. 3, 2019. URL https://www.mdpi.com/2226-4310/6/3/27.

[28] Khalil, A., and Fezans, N., "Performance Enhancement of Gust Load Alleviation Systems for Flexible Aircraft using H∞ Optimal Control with Preview," *AIAA Scitech 2019 Forum*, American Institute of Aeronautics and Astronautics, 2019. https://doi.org/10.2514/6.2019-0822.

[29] Fournier, H., Massioni, P., Tu Pham, M., Bako, L., Vernay, R., and Colombo, M., "Robust Gust Load Alleviation of Flexible Aircraft Equipped with Lidar," *Journal of Guidance, Control, and Dynamics*, Vol. 0 (Future Release), No. 0, 2021, pp. 1–15. https://doi.org/10.2514/1.G006084.

[30] Zeng, J., Moulin, B., de Callafon, R., and Brenner, M. J., "Adaptive Feedforward Control for Gust Load Alleviation," *Journal of Guidance, Control, and Dynamics*, Vol. 33, No. 3, 2010, pp. 862–872. https://doi.org/10.2514/1.46091.

[31] Wildschek, A., Maier, R., Hoffmann, F., Steigenberger, J., Kaulfuss, K.-H., Breitsamter, C., Allen, A., Adams, N., Baier, H., Giannopoulos, T., and Dafnis, A., "Wind Tunnel Testing of an Adaptive Control System for Vibration Suppression on Aircraft," *AIAA Guidance, Navigation and Control Conference and Exhibit*, American Institute of Aeronautics and Astronautics, 2007. https://doi.org/10.2514/6.2007-6331.

[32] Wang, Y., Li, F., and Ronch, A. D., "Adaptive Feedforward Control Design for Gust Loads Alleviation of Highly Flexible Aircraft," *AIAA Atmospheric Flight Mechanics Conference*, American Institute of Aeronautics and Astronautics, 2015. https://doi.org/10.2514/6.2015-2243.

[33] Apkarian, P., Noll, D., and Rondepierre, A., "Mixed H2/H-infinity control via nonsmooth optimization," *Proceedings of the 48h IEEE Conference on Decision and Control (CDC) held jointly with 2009 28th Chinese Control Conference*, 2009, pp. 6460–6465. https://doi.org/10.1109/CDC.2009.5400165.

[34] MSC.Software Corporation, *MSC.Nastran Version 68, Aeroelastic Analysis User's Guide*, 2004, pp. 26–126.

[35] U.S. Government Printing Office, Washington, D.C., "U.S. Standard Atmosphere, 1962," , 1962. URL https://ntrs.nasa.gov/citations/19630003300.

[36] Lefteriu, S., and Antoulas, A. C., "A New Approach to Modeling Multiport Systems From Frequency-Domain Data," *IEEE Transactions on Computer-Aided Design of Integrated Circuits and Systems*, Vol. 29, No. 1, 2010, pp. 14–27. https://doi.org/10.1109/tcad.2009.2034500.

[37] Mayo, A., and Antoulas, A., "A framework for the solution of the generalized realization problem," *Linear Algebra and its Applications*, Vol. 425, No. 2-3, 2007, pp. 634–662. https://doi.org/10.1016/j.laa.2007.03.008.

[38] Karachalios, D., Gosea, I., and Antoulas, A., *The Loewner framework for system identification and reduction*, De Gruyter, 2019. https://doi.org/10.1515/9783110498967-006.

[39] European Aviation Safety Agency (EASA), "Certification Specifications for Large Aeroplanes, Amendment 3," , 09 2007. URL https://www.easa.europa.eu/sites/default/files/dfu/CS-25_Amdt%203_19.09.07_Consolidated%20version.pdf.

[40] Diederich, F., and Drischler, J., *Effect of Spanwise Variations in Gust Intensity on the Lift Due to Atmospheric Turbulence*, Technical note, National Advisory Committee for Aeronautics, 1957.

[41] Apkarian, P., Dao, M. N., and Noll, D., "Parametric Robust Structured Control Design," *IEEE Transactions on Automatic Control*, Vol. 60, No. 7, 2015, pp. 1857–1869. https://doi.org/10.1109/TAC.2015.2396644.